Appl Biochem Biotechnol
DOI 10.1007/s12010-014-0997-9

Synthesis and Characterization of Reduced Graphene Oxide Supported Gold Nanoparticles-Poly (Pyrrole-Co-Pyrrolepropylic Acid) Nanocomposite-Based Electrochemical Biosensor

Nidhi Puri · Asad Niazi · Avanish K. Srivastava · Rajesh

Received: 13 January 2014 / Accepted: 22 May 2014

Abstract A conducting poly(pyrrole-co-pyrrolepropylic acid) copolymer nanocomposite film (AuNP-PPy-PPa) incorporating gold nanoparticles (AuNP) was electrochemically grown using a single step procedure over electrochemically reduced graphene oxide (RGO) flakes deposited on a silane-modified indium-tin-oxide (ITO) glass plate. The RGO support base provided excellent mechanical and chemical stability to the polymer nanocomposite matrix. The porous nanostructure of AuNP-PPy-PPa/RGO provided a huge accessible area to disperse AuNP, and it avoided metallic agglomeration within the polymer matrix. The AuNP-PPy-PPa/RGO was characterized by high-resolution transmission electron microscopy (HRTEM), contact angle measurements, Fourier transform infrared spectroscopy (FTIR), and electrochemical techniques. The pendant carboxyl group of AuNP-PPy-PPa/RGO was covalently bonded with myoglobin protein antibody, Ab-Mb, for the construction of a bioelectrode. Electrochemical impedance spectroscopy technique was used for the characterization of the bioelectrode and as an impedimetric biosensor for the detection of human cardiac biomarker, Ag-cMb. The bioelectrode exhibited a linear impedimetric response to Ag-cMb in the range of 10 ng mL^{-1} to 1 μg mL^{-1}, in phosphate-buffered solution (PBS) (pH 7.4, 0.1 M KCl) with a sensitivity of 92.13 Ω cm^2 per decade.

Keywords Conducting polymer · Electrochemical sensing · Graphene · Immunoreaction · Antibody

Introduction

Carbon nanomaterials, such as carbon nanotubes, fullerenes, and graphene are of great interest in the scientific community because of their unique physicochemical properties and

N. Puri · A. K. Srivastava · Rajesh (✉)
CSIR-National Physical Laboratory, Dr. K.S. Krishnan Road, New Delhi 110012, India
e-mail: rajesh_csir@yahoo.com

N. Puri · A. Niazi
Department of Physics, Faculty of Natural Sciences, Jamia Millia Islamia, New Delhi 110025, India

Published online: 14 June 2014

extraordinary conductivities which facilitate in designing of sensors and fuel cells [1–3]. Graphene has emerged as a novel nanomaterial for electrochemistry because of its flexibility, large surface to volume ratio, robust mechanical properties, and good electrical and thermal conductivity which provides easier electron mobility and novel electron transfer properties at room temperature [4–6]. Electrochemically reduced graphene oxide (RGO), a precursor of graphene, is widely used in biosensing applications [7–9]. Its large accessible surface area allows high loading of biomolecules, and its small band gap and excellent electrical conductivity [10] provide ease of conduction of electrons from biomolecules, leading to much higher sensitivity of the bioelectrode. Semiconductor and metal nanoparticle (MNP) (Ag, Au, and Pt)-decorated graphene is increasingly being used in electronic devices and sensing applications [11–14]. Although MNPs/graphene hybrids have shown wider applications, there remain a number of concerns such as (i) the difficulty of dense connection between MNPs and the graphene layer; (ii) the nonuniform dispersion of MNPs over graphene sheets; and (iii) low biocompatibility, since graphene's two dimensional structure [15] has functional groups available only at its edges which reduces its interaction with MNPs, resulting in low sensitivity [16].

Conducting polymers have been used as biomolecular probe immobilizing matrices for the last two decades. Their organized molecular structure supported on rigid substrates permits them to function as three-dimensional matrices to immobilize and preserve the activity of biomolecules for long duration [17]. Polypyrrole (PPy), the most promising conducting polymer (CP), has been used widely in biosensing applications due to its excellent stability, conductivity, and biocompatibility [18–20]. In addition, CPs provide high-accessible surface area for the uniform distribution of MNPs in polymer nanocomposites used in various applications [21, 22]. However, better probe immobilization on the hydrophobic PPy surface is a challenge due to the poor accessibility of the targeted biomolecule. Firm connection of the probe biomolecules in proper orientation on the polymer matrix can be achieved through covalent biomolecular immobilization either by post-functionalization of the PPy surface or initial polymerization of carboxyl pendant (prefunctionalized) pyrrole derivatives. Our previous work [23] showed that a copolymer of pyrrole and pyrrolepropylic acid (Pa) facilitated a compact probe immobilization with high probe density through covalent binding.

Acute myocardial infarction (AMI) leads to decrease or stoppage of blood flow to the heart muscle tissue, causing cell death. Myoglobin (cMb), not cardiac-specific, is one of the biomarkers released immediately upon an AMI, and its rapid screening under acute physiological conditions is fundamental to AMI diagnosis [24, 25]. The "cutoff" concentrations of small-sized (17.8 kDa) cMb may vary from 50 ng mL^{-1} (Behring Diagnostics method, Nanogen cardiac STATus panel) and 56 ng mL^{-1} (Stratus CS STAT, for female) to 170–200 ng mL^{-1} (Triage Cardiac Panel [26]). The enzyme-linked immunosorbent assay (ELISA) [27] and chromatographic [28] or spectrophotometric [29] tests are some of the available methods for the quantitative detection of cMb. However, these methods suffer from disadvantages of time consuming and complex preparatory methods. Instead, electrochemical impedance spectroscopy (EIS) using appropriate bioelectrodes has been found to be a rapid, nondestructive, and sensitive detection technique.

In this work, we report the synthesis and electrochemical impedance sensing behavior of electrochemically reduced graphene oxide (RGO)-based copolymer nanocomposite bioelectrode. Gold nanoparticle (AuNP)-incorporated conducting poly(pyrrole-co-pyrrolepropylic acid) (PPy-PPa) copolymer film was electrochemically grown over RGO-based silane-modified indium tin oxide (ITO) glass plate for the preparation of a bioelectrode useful for the quantitative detection of human cardiac myoglobin (cMb). While there have been earlier studies on nanocomposite materials of RGO with PtNP [30] and AuNP [31] as electrochemical sensors, no one has yet reported the importance of AuNP nanocomposites

with RGO-based conducting polymers in electrochemical biosensors. In the present work, the RGO matrix provided conducting, mechanical, and chemical stability to the AuNP-PPy-PPa polymer nanocomposite for biomolecular immobilization though covalent bonding and imparted an ease of electron transport with accessible surface area for a better probe orientation. The EIS sensing performance of the above bioelectrode was evaluated for the quantitative detection of target Ag-cMb in phosphate-buffered solution (PBS; pH 7.4, 0.1 M KCl). The synergistic characteristic of both RGO and AuNP in the copolymer film was investigated with respect to native PPy-PPa copolymer film in terms of the overall performance of the bioelectrode.

Materials and Methods

Chemicals and Reagents

Ag-cMb (Cat 8 M50) and Ab-cMb (4 M23) were obtained from Hytest (Turku, Finland). Mouse immunoglobulin-G (Ag-IgG) (Cat IGP3) was obtained from Genei, Bangalore. 3-Aminopropyltriethoxysilane (APTES) was purchased from Merck Chemicals (Germany). Tetrachloroauric(III) acid ($HAuClO_4$) was obtained from Him Media Pvt. Ltd. Pyrrole, pyrrolepropylic acid, sodium *p*-Toluenesulfonic acid (*p*-TSA), *N*-(3-dimethylaminopropyl)-*N*′-ethyl carbodiimide hydrochloride (EDC) and *N*-hydroxysuccinimide (NHS) 98 %, were obtained from Sigma-Aldrich chemicals. All other chemicals were of analytical grade and used without further purification.

Apparatus

Microstructural characterization was performed with a high-resolution transmission electron microscopy (HRTEM model Tecnai G2 F30 STWIN with field emission gun, operated at 300 kV). Contact angle measurements were studied on an apparatus provided by Drop Shape Analysis System, model DSA10MK2 from Kruss GmbH, Germany. Fourier transform infrared (FTIR) spectrum was taken on PerkinElmer, Spectrum BX II. Cyclic voltammetry (CV) and EIS measurements were done on a PGSTAT302N, Autolab instrument from Eco Chemie, The Netherlands. The CV and EIS measurements were carried out in PBS (pH 7.4, 0.1 M KCl) containing a mixture of 2 mM $K_3[Fe_3(CN)_6]$ and 2 mM $K_4[Fe_2(CN)_6]$. The EIS experiments were carried out at a bias voltage of 0.3 V and an ac voltage of 0.05 V in the frequency range of 1 Hz to 100 kHz. A conventional three-electrode cell configuration consisting of AuNP-PPy-PPa/RGO/APTES/ITO glass as a working electrode, Ag/AgCl reference electrode, and platinum counter electrode was used throughout the experiment.

Preparation of Biofunctionalized Copolymer Nanocomposite Film

The ITO-coated glass plates were sequentially cleaned in extran (soap solution), acetone, ethanol, 2-propanol, and double-distilled water, each for 10 min and dried under N_2 gas flow. The cleaned ITO glass plates were exposed to oxygen plasma for 5 min in a plasma chamber and then immersed for 1.5 h in 2 % APTES solution prepared in ethanol, under ambient conditions, to form a self-assembled monolayer of APTES. The glass plates were then rinsed with ethanol to remove nonbonded APTES molecules from the surface of the substrate and dried under N_2 gas flow. The APTES-modified ITO glass plates were masked with insulating tape, leaving open a working area of 0.25 cm^2 on each plate, immersed in sonicated GO

aqueous suspension (0.3 mg mL^{-1}) for a period of 1 h to enable the electrostatic attachment of negatively charged GO sheets over the positively charged APTES-modified ITO glass, and then washed with distilled water and dried under N_2 flow to form the GO/APTES/ITO glass electrodes. These GO-modified electrodes were electrochemically reduced by CV, in a potential window of 0.1 to −1.1 V for three CV cycles, at a scan rate of 50 mV s^{-1}, in 0.5 M degassed (N_2 purged) KCl aqueous solution to obtain the RGO/APTES/ITO glass electrodes. The electrochemical reduction process is given by Eq. (1):

$$GO + aH^{-} + be^{-} \rightarrow RGO + H_20 \quad (1)$$

Figure 1 shows that the GO rapidly reduces in the very first CV cycle with a reduction peak at −1.1 V. In subsequent cycles, it completely disappeared, indicating the elimination of the vast majority of oxygenated functional groups such as alchohol, ketone, epoxides, lactol, and ester from the structure of GO [32].

The AuNPs were synthesized in an aqueous solution of $HAuCl_4$ at room temperature by a method reported earlier [33]. The AuNP-PPy-PPa copolymer nanocomposite film was electrochemically prepared on the above RGO/APTES/ITO glass electrodes in a single step electropolymerization method using a degassed (N_2 purged) aqueous solution of 0.1 M pyrrole, 0.03 M pyrrolepropylic acid, 0.1 M PTSA, and 0.2 mg mL^{-1} AuNP, at a fixed current density of 1 mA cm^{-2} with an injected charge density of 100 mC cm^{-2}. The prepared polymer electrode was biofunctionalized with human cardiac myoglobin protein antibody, Ab-Mb, in two steps: (i) activating the AuNP-PPy-PPa film with an aqueous solution containing 30 mM NHS:150 mM EDC (1:5) for 1 h and (ii) treating the activated film with PBS (pH 7.4) containing 100 μg mL^{-1} Ab-cMb, for a period of 3 h at 4 °C, followed by washing with PBS and drying under N_2 gas flow to obtain the Ab-Mb-AuNP-PPy-PPa/RGO/APTES/ITO glass bioelectrode. The bioelectrode was then treated with 1 % bovine serum albumin (BSA) in PBS for 30 min to block the nonspecific binding sites, if any, on the electrode surface, followed by

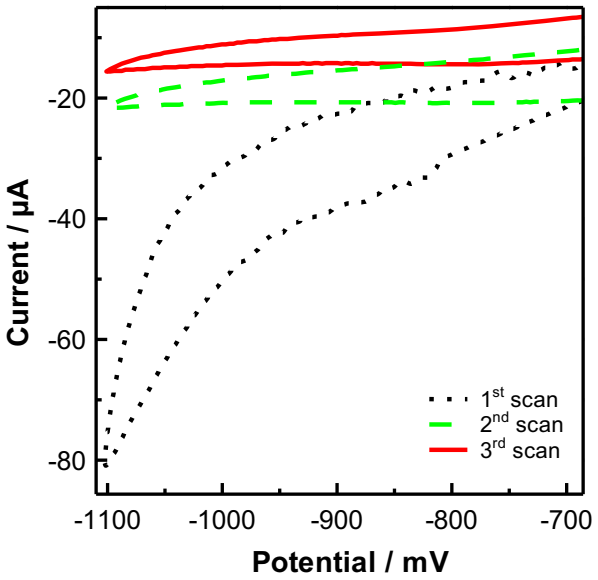

Fig. 1 Electrochemical reduction of GO/APTES/ITO glass plate in a degassed solution of 0.5 M KCl at a scan rate of 50 mV s^{-1}

washing with PBS and drying under N_2 flow. The Ab-Mb(BSA)-AuNP-PPy-PPa/RGO/APTES/ITO glass bioelectrode was stored at 4 °C when not in use. The schematic presentation of the bioelectrode is given in Scheme 1.

Results and Discussion

Microstructural Characterization of the AuNP-PPy-PPa/RGO Nanocomposite

HRTEM was used for microstructural characterization of the AuNP-PPy-PPa/RGO-based electrode. Several features of AuNP (size ranging between 3 and 6 nm) dispersed in the nanocomposite matrix of RGO, and PPy-PPa were examined and interpreted. It was observed that the AuNPs were merged with the matrix in such a way that it was difficult to distinguish a clear boundary of Au with the matrix. Figure 2a–d reveal some of the interesting findings of this composite material. Figure 2a is a low-magnification image showing the broad distribution of the dark gray AuNP regions in the AuNP-PPy-PPa/RGO nanocomposite. Since it is in composite with other materials, the boundaries of AuNPs are not so distinguishable and obvious. However, the impressions of AuNPs in several regions have been marked. A differentiate image of the honeycomb-hexagonal network of RGO is discerned in Fig. 2b showing an interplanar spacing of about 0.34 nm. Figure 2c shows the AuNP-RGO interface. We observe that the gold (with a bulk fcc crystal structure, space group: Fm $\overline{3}$ m, lattice parameter: a= 0.408 nm) is stacked along 111 planes with interplanar spacing of 0.24 nm, adjacent to RGO planes with interplanar spacing of 0.34 nm. For further clarity, Fig. 2d reveals a well-defined AuNP along with GO and PPy-PPa with a dark gray level contrast, at lattice scale.

Contact angle measurement is an important parameter to study the surface hydrophobic and hydrophilic character of the matrix. The liquid sessile drop method was used to determine the contact angle of the matrix at each step of surface modification. The image of the drop deposited on the modified electrode surface was recorded by a video camera with an initial waiting period of 10 s to stabilize the drop on the surface. An image analysis system was used to calculate the contact angle (θ) from the shape of the drop. All measurements were repeated with four drops of ultrapure water, at different regions of the modified surface (Fig. 3). The low contact angle value of ITO glass electrode (40.44°) (Fig. 3a) was found to increase to 65.44° (Fig. 3b) upon modification with the self-assembled monolayer (SAM) of APTES, due to the surface hydrophobic alkyl chains of APTES molecules. The APTES/ITO glass electrode became less hydrophobic after the electrostatic attachment of the GO flakes to APTES where the oxygenated hydrophilic groups like –OH and –COOH reduce the contact angle to 56.22° (Fig. 3c). However, upon electrochemical reduction of GO to RGO, the surface again became hydrophobic with a contact angle of 77.49° (Fig. 3d) due to the reduction of the surface oxygenated groups. The electrodeposition of AuNP-PPy-PPa with hydrophilic pendant

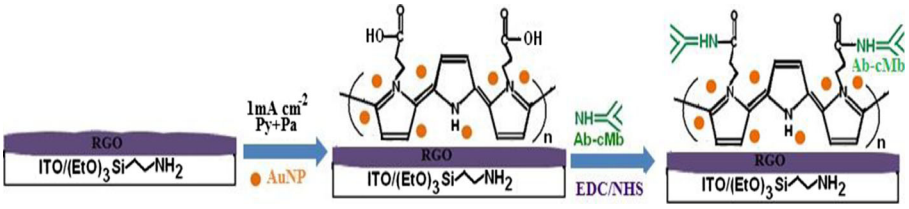

Scheme 1 Schematic representation of the stepwise fabrication of the bioelectrode

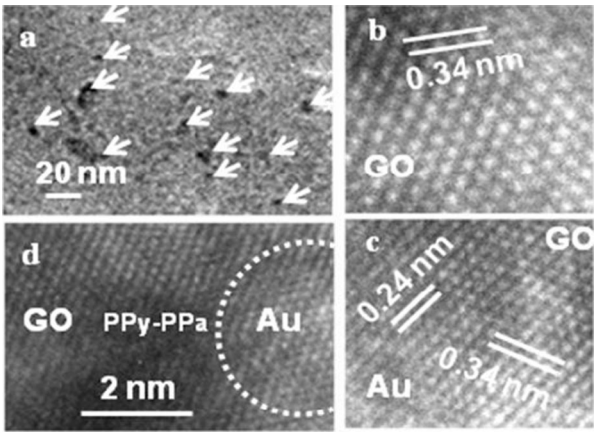

Fig. 2 HRTEM micrographs showing AuNP distributed in GO and PPy-PPa matrix. Few AuNP are encircled by *white dotted line*. **a** Low magnification image of AuNP dispersion in the matrix, **b** RGO at atomic scale, **c** atomic scale image of the interface between Au and RGO, and **d** a composite atomic scale micrograph of Au, RGO, and PPy-PPa

carboxyl group over the RGO surface led to a small decline in the hydrophobic character with a contact angle of 70.15°, followed by an increasing hydrophobic nature with a contact angle of 87.22° upon covalent immobilization of the hydrophobic protein antibody molecules.

The composite formation was further confirmed by taking FTIR spectra of composite both before and after biomolecular immobilization (Fig. 4). The FTIR spectra of AuNP-PPy-PPa/RGO composite showed two distinctive peaks at 1,730 and 1,030 cm^{-1} ascribed to carboxyl groups and epoxy ring of RGO, respectively [34] with characteristic PPy peaks at about 1,435 and 1,541 cm^{-1} indicative of asymmetric and symmetric ring stretching modes in the backbone structure of pyrrole unit [35]. The appearance of the N–H stretching band at around 3,390 cm^{-1} corresponding to the amide band [36] confirmed the biomolecular immobilization of the polymer nanocomposite with Ab-Mb.

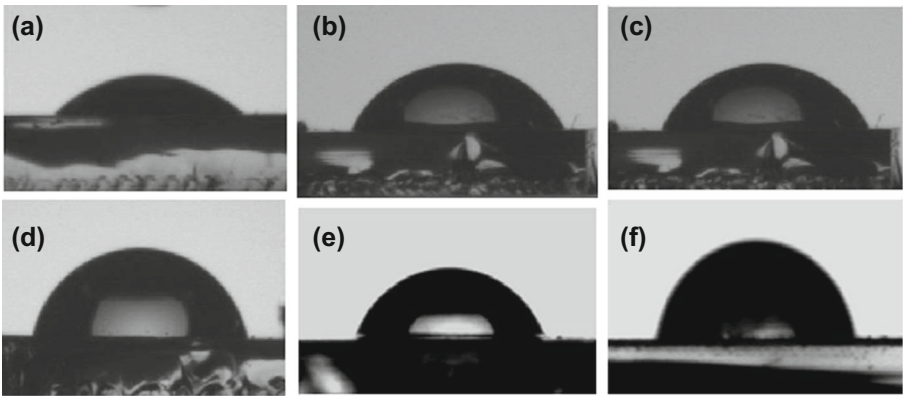

Fig. 3 Contact angle images of DI water on ITO glass showing hydrophilic/hydrophobic surface properties: **a** ITO glass, **b** APTES/ITO glass, **c** GO/APTES/ITO glass, **d** RGO/APTES/ITO glass, **e** AuNP-PPy-PPa/RGO/APTES/ITO glass, and **f** Ab-Mb/AuNP-PPy-PPa/RGO/APTES/ITO glass electrodes

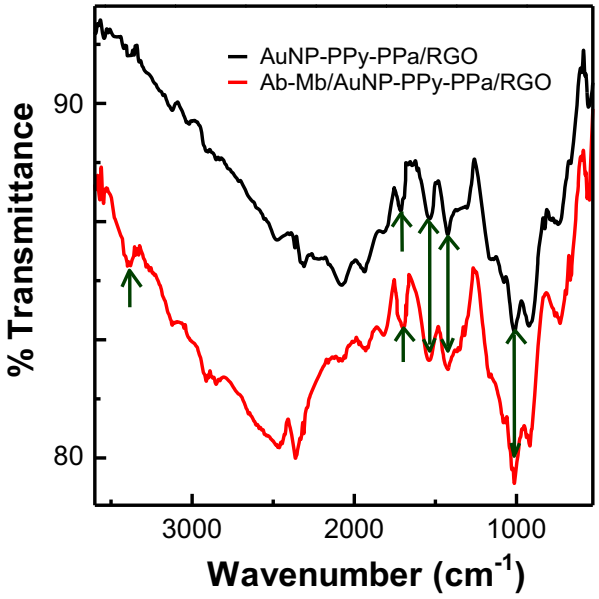

Fig. 4 FTIR spectra of AuNP-PPy-PPa/RGO and Ab-Mb/AuNP-PPy-PPa/RGO

Electrochemical Characterization of the Bioelectrode

Methods such as EIS and CV are powerful tools for probing the electrochemical interfacial properties and characterizing the surface of modified electrodes. EIS works on a small amplitude sinusoidal ac signal in a wide frequency range and provides a complete description of the electrochemical system in terms of capacitances, resistances, and impedances by fitting the experimental data, i.e., Nyquist plots (real part (Z′) versus imaginary part (−Z″) of the impedance) (Fig. 5) to the Randles equivalent circuit (inset of Fig. 5a). The circuit elements are as follows: (i) the ohmic resistance of the electrolyte solution, R_s; (ii) the electron or charge transfer resistance, R_{et}; (iii) the Warburg impedance, W_R, resulting from the diffusion of ions from the bulk electrolyte to the electrode interface; and (iv) the constant phase element (CPE) indicating the degree of surface roughness, inhomogeneity, and electrode porosity. The impedance due to CPE can be expressed by Eq. (2):

$$Z_{(CPE)} = 1/Q_0(j\omega)^{-n} \tag{2}$$

where Q_0 is the constant, j is $\sqrt{(-1)}$, ω is the angular frequency, and n is the dimensional CPE exponent ($n \leq 1$) indicating the degree of surface inhomogeneity or roughness. A variation in the value of n from 0.53 to 0.86 indicated an enhanced surface inhomogeneity for the AuNP-PPy-PPa/RGO composite in comparison to the earlier reported native PPy-PPa surface [23] where C_{dl} was used to describe the equivalent circuit that fitted the experimental value.

The Nyquist plots exhibit a semicircular region with diameter R_{et} at high frequencies and a straight line at lower frequencies. The semicircle corresponds to R_s, R_{et}, and capacitance of the electrochemical cell while the straight region represents the diffusion-limited transport of the redox species from the electrolyte to the electrode interface. R_s and W_R are related to the electrolyte solution properties and diffusion of the bulk electrolyte ions to the electrode

interface, respectively. Since negligible changes were observed for R_s and W_R in comparison to the R_{et}, R_{et} was chosen as a major element to characterize the electrode solution interfacial properties at various stages of surface modification. The experimental data was found to be in good agreement with the fitted circuit model with $\chi^2 \sim 10^{-4}$ (Table 1).

An R_{et} value of 344 Ω cm^2 was obtained for silane-modified ITO glass electrode indicating easy electronic transport between the positively charged amine groups and the negatively charged redox probe at the electrode surface. Upon electrostatic deposition of negatively charged GO flakes over the positively charged amine groups of the silane-modified ITO glass electrode, this R_{et} value increased to 594 Ω cm^2. This is because oxygenated groups like COOH/OH$^-$ at the GO surface create electrostatic repulsion at the electrode-solution interface (Table 1). The R_{et} decreased to 466 Ω cm^2 upon electrochemical reduction to RGO. A dramatic fall in R_{et} to 3.51 Ω cm^2 was observed after the electrodeposition of AuNP-PPy-PPa on RGO due the electron conduction provided by the positive charges generated on the polymer nanocomposite surface at a bias voltage of 0.3 V. It is interesting to note here that these results reveal positive charge carriers as a dominant factor over the negatively charged pendant−COOH groups of the PPa moiety for easy electron transport at the electrode solution interface. However, a high R_{et} value of 30.85 Ω cm^2 was observed upon covalent immobilization of the protein antibody, Ab-Mb, on the AuNP-PPy-PPa/RGO nanocomposite film, which may be attributed to the insulating protein molecules, hindering interfacial electron transfer.

The heterogeneous electron transfer rate constant value (k^0) of redox probe is another important factor to further confirm the faster and easier electronic transport process occurring at the polymer nanocomposite film. According to charge transfer kinetics, k^0 is expressed by

$$k^0 = \mathrm{RT}/{n_1}^2\mathrm{F}^2\mathrm{A}R_{et}\mathrm{C} \tag{3}$$

where R is the gas constant, T is the temperature, n_1 is the number of electrons involved in the electrode reaction, F is Faraday constant, A is the area of electrode (0.25 cm^2), and C is the concentration of the redox probe in the bulk solution. The k^0 values of the modified electrode during different stages of preparation are given in Table 1. A remarkably large k^0 value of 37.89×10^{-4} m s^{-1} was obtained for AuNP-PPy-PPa nanocomposite film electrodeposited over RGO in comparison to 0.28×10^{-4} m s^{-1} for the RGO matrix. This may correspond to the combined conduction characteristics of both the PPy-PPa and AuNP in the polymer nanocomposite film which therefore exhibits enhanced ionic as well as electron transport. Upon subsequent protein Ab-Mb immobilization, a significant fall in k^0 value (3.54×10^{-4} m s^{-1}) indicated sluggish electron transport resulting from the insulating feature of the protein molecules, confirming the formation of the bioelectrode.

The above results are more evident in the frequency-dependent bode plots (Fig. 5b) of the bioelectrode which relate the logarithm of frequency (Log f) to the logarithm of magnitude of impedance (Log |Z|) and negative of phase angle (Φ). The bode plots provide information about kinetics occurring at the electrode/solution interface, at a wide range of applied frequencies. The RGO-modified electrode showed capacitive characteristics in the frequency range of 10 to 3,000 Hz with a R_{et} feature at <10 Hz frequency. Significant changes were observed both in capacitive and R_{et} behavior of the electrodeposited AuNP-PPy-PPa/RGO. The capacitance feature shifted toward the high frequency region of 3 to 30 kHz with a major fall from Q_0=37.92 to 1.38 μF cm^{-2}, while the R_{et} characteristic was obtained in a wide frequency region of 10 Hz to 1 kHz with a minimum in the phase angle where I/t is nearly in phase with v/t. It is interesting to note that the AuNP-PPy-PPa/RGO showed a very prominent diffusive characteristic feature with almost linear Log |Z| in the low frequency region of 1 to 10 Hz. This diffusive characteristic may be attributed to the porous and inhomogenous surface of the polymer nanocomposites as supported by a comparatively low value

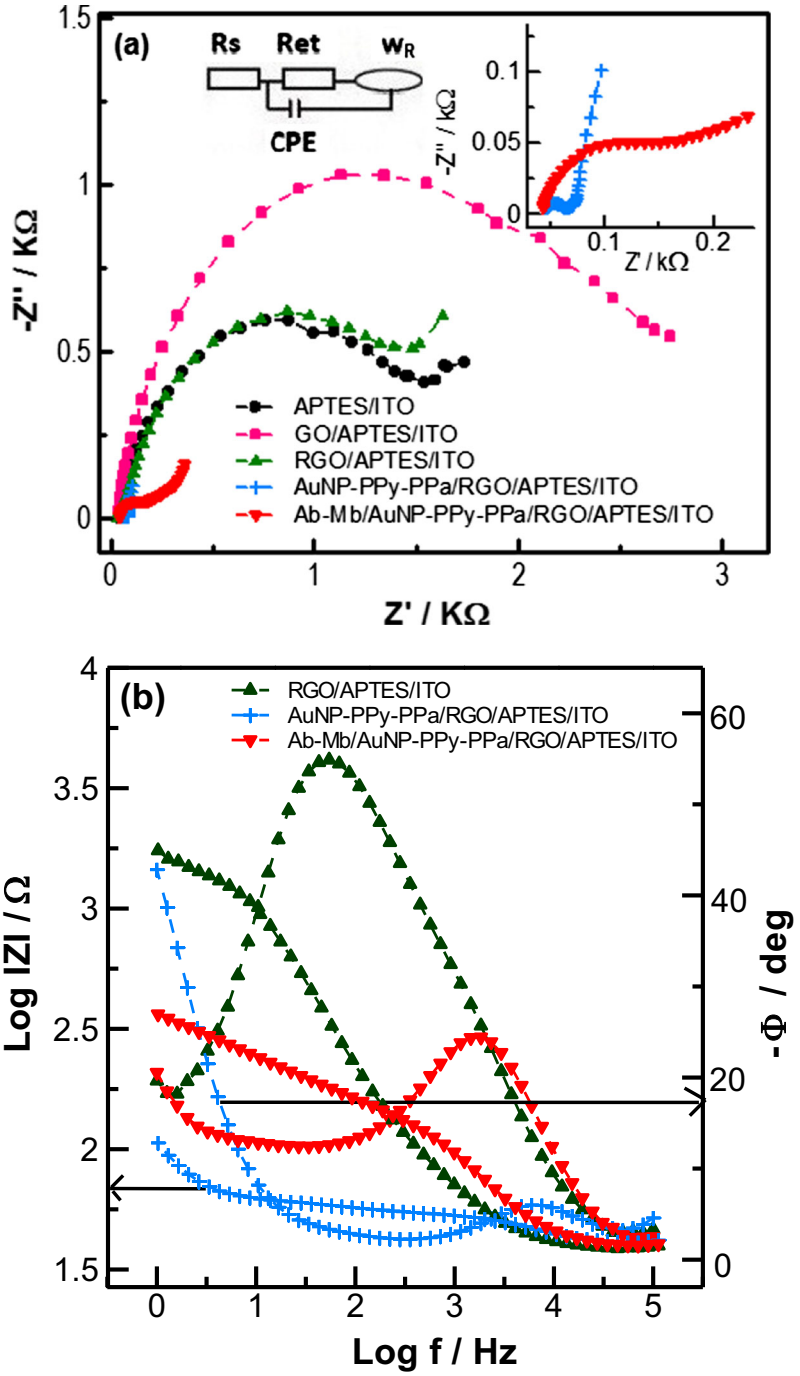

Fig. 5 **a** Nyquist plot for APTES/ITO glass, GO/APTES/ITO glass, RGO/APTES/ITO glass, AuNP-PPy-PPa/RGO/APTES/ITO glass, and Ab-Mb/AuNP-PPy-PPa/RGO/APTES/ITO glass in PBS (pH 7.4, 0.1 M KCl) containing 2 mM $[Fe(CN)_6]^{3-/4-}$; *inset*: Nyquist plot for AuNP-PPy-PPa/RGO/APTES/ITO glass and Ab-Mb/AuNP-PPy-PPa/RGO/APTES/ITO glass and Randles equivalent circuit; and **b** corresponding bode plots

of n=0.54. Upon Ab-Mb immobilization on the polymer nanocomposite film, the R_{et} characteristic shifted toward the low frequency region of 3 to 300 Hz with almost a negligible diffusive characteristic. This may correspond to a more compact and homogenous surface for Ab-Mb/AuNP-PPy-PPa/RGO, also suggested by a comparatively high value of n=0.68 with respect to an AuNP-PPy-PPa/RGO film, leading to the formation of a bioelectrode.

The charge transfer properties occurring at the bioelectrode surface were characterized by CV at different scan rates in the range 25–125 mV s^{-1}. The $[Fe(CN)_6]^{3-/4-}$ redox couple behaves like a benchmark to characterize charge transfer properties due to its sensitivity to the surface chemistry. Figure 6 shows CV cycles of the bioelectrode taken at different scan rates with the inset showing a linear change in cathodic peak current (I_{pc}) as a function of square root of the scan rate ($\nu^{1/2}$). This linear behavior suggests that the electrochemical reaction occurring at the bioelectrode surface is a semiinfinite linear diffusion controled process [37]. The linear relationship between the redox peak current I_{pc} and $\nu^{1/2}$ is given by

$$I_{pc}\left(v^{1/2}\right) = bv^{1/2} - 27.12 \tag{4}$$

where the slope $b = -3.74 \times 10^{-6} \pm 0.02\ \mu A (mV\ s^{-1})^{-1/2}$ with a correlation coefficient of 0.996.

EIS Response Studies of the Bioelectrode Toward the Protein Ag-cMb

The EIS measurement was performed after dispensing 10 μL of the individual sample of different Ag-cMb concentrations on the bioelectrode surface and allowing it to react with the complementary Ab-Mb for 10 min to complete the immunoreaction at room temperature. Since no significant change in the EIS signal was observed after more than 10 min of incubation time, we accepted this as an optimized response time for the completion of immunoreactions at the bioelectrode surface. The bioelectrode was then washed with PBS and dried under N_2 gas flow. The EIS-fitted experimental data are given in Table 2. Figure 7 shows the EIS spectra (Nyquist plot and bode plot) of the Ab-Mb(BSA)-AuNP-PPy-PPa/RGO/APTES/ITO glass bioelectrode after dispensing different concentrations of Ag-cMb in PBS (pH 7.4, 0.1 M KCl) on the bioelectrode surface. The Nyquist plot (Fig. 7a) shows an increasing trend in the R_{et} values of the bioelectrode with the increasing concentration of Ag-cMb with respect to a control sample solution containing no Ag-cMb. This increase in R_{et} is assigned to an antigen-antibody complex formation on immunoreaction, producing a kinetic barrier which perturbs the interfacial electron transport at the bioelectrode surface.

Table 1 EIS characteristic parameters at various stages of surface modifications of the electrode

Electrodes	R_{et} (Ω cm^2)	CPE		W_R (Ω cm^2)	k^0 ($m\ s^{-1}$)	χ^2 (10^{-4})
		Z_0 (μF cm^{-2})	n			
APTES/ITO glass	344	7.80	0.869	0.18×10^{-3}	0.38×10^{-4}	2.32
GO/APTES/ITO glass	593.50	5.28	0.912	0.20×10^{-3}	0.22×10^{-4}	3.05
RGO/APTES/ITO glass	466.75	37.92	0.744	1.10×10^{-3}	0.28×10^{-4}	1.52
AuNP-PPy-PPa/RGO/APTES/ITO glass	3.51	1.38	0.542	1.25×10^{-3}	37.89×10^{-4}	4.16
Ab-Mb/AuNP-PPy-PPa/RGO/APTES/ITO glass	37.62	17.98	0.686	0.36×10^{-3}	3.53×10^{-4}	7.57

R_{et} charge transfer resistance, *CPE* constant phase element, W_R Warburg impedance, k^0 apparent rate constant

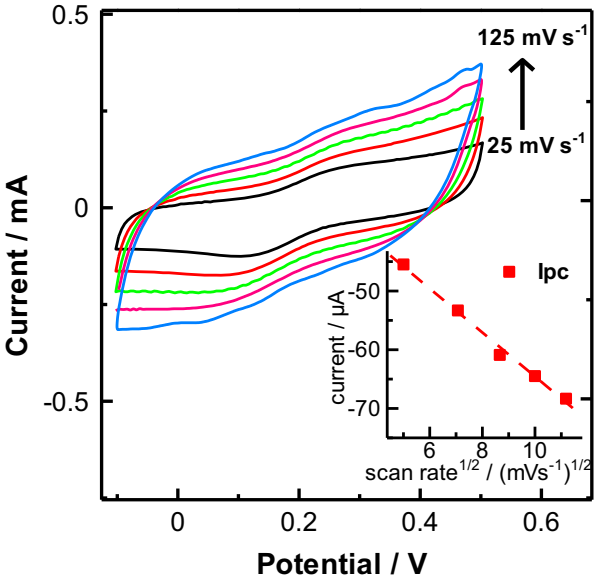

Fig. 6 CV of bioelectrode as a function of scan rate in PBS (pH 7.4, 0.1 M KCl) containing 2 mM $[Fe(CN)_6]^{3-/4-}$ at scan rate of 25 to 125 mV s^{-1}; *inset*: plot of cathodic peak current I_{pc} versus $v^{1/2}$

These results are further elaborated with the frequency-dependent bode plots (Fig. 7b) of the bioelectrode. The bode plot obtained for the bioelectrode can be explained by dividing the frequency region under three sections, i.e., (i) high frequency region (>10 kHz) where impedance is independent of frequency with a nearly zero phase angle (Φ), corresponding to a solution resistance, R_s; (ii) the mid frequency region of 100 Hz to 10 kHz, which is dominated by a pseudo capacitive element CPE with a subsequent increase in the phase angle from 30° to 60° on immunoreaction with increasing Ag-cMb concentration; and (iii) low frequency region of <100 Hz, where the *I*/*t* and *V*/*t* are nearly in phase (i.e., least phase angle) signifying the frequency independence of the charge transfer characteristics (R_{et}) and the diffusion controled process (W_R) of the bioelectrode. All of the major changes in the overall

Table 2 EIS parameters of the bioelectrode on immunoreaction with different concentrations of Ag-cMb in PBS (pH 7.4)

Immunoreaction with Ag-cMb	R_{et} (Ω cm^2)	CPE		W_R (Ω cm^2)	χ^2 (10^{-4})
		Z_0 (µF cm^{-2})	n		
Control	37.62	17.98	0.686	0.36×10^{-3}	7.57
0.001 µg mL^{-1}	66.52	9.39	0.799	0.37×10^{-3}	4.98
0.01 µg mL^{-1}	86.50	6.45	0.841	0.39×10^{-3}	3.20
0.05 µg mL^{-1}	112.75	5.44	0.862	0.41×10^{-3}	3.08
0.10 µg mL^{-1}	155	4.83	0.877	0.42×10^{-3}	5.43
0.50 µg mL^{-1}	217	4.46	0.887	0.42×10^{-3}	4.74
1.00 µg mL^{-1}	270.5	4.23	0.895	0.43×10^{-3}	6.69

R_{et} charge transfer resistance, *CPE* constant phase element, W_R Warburg impedance

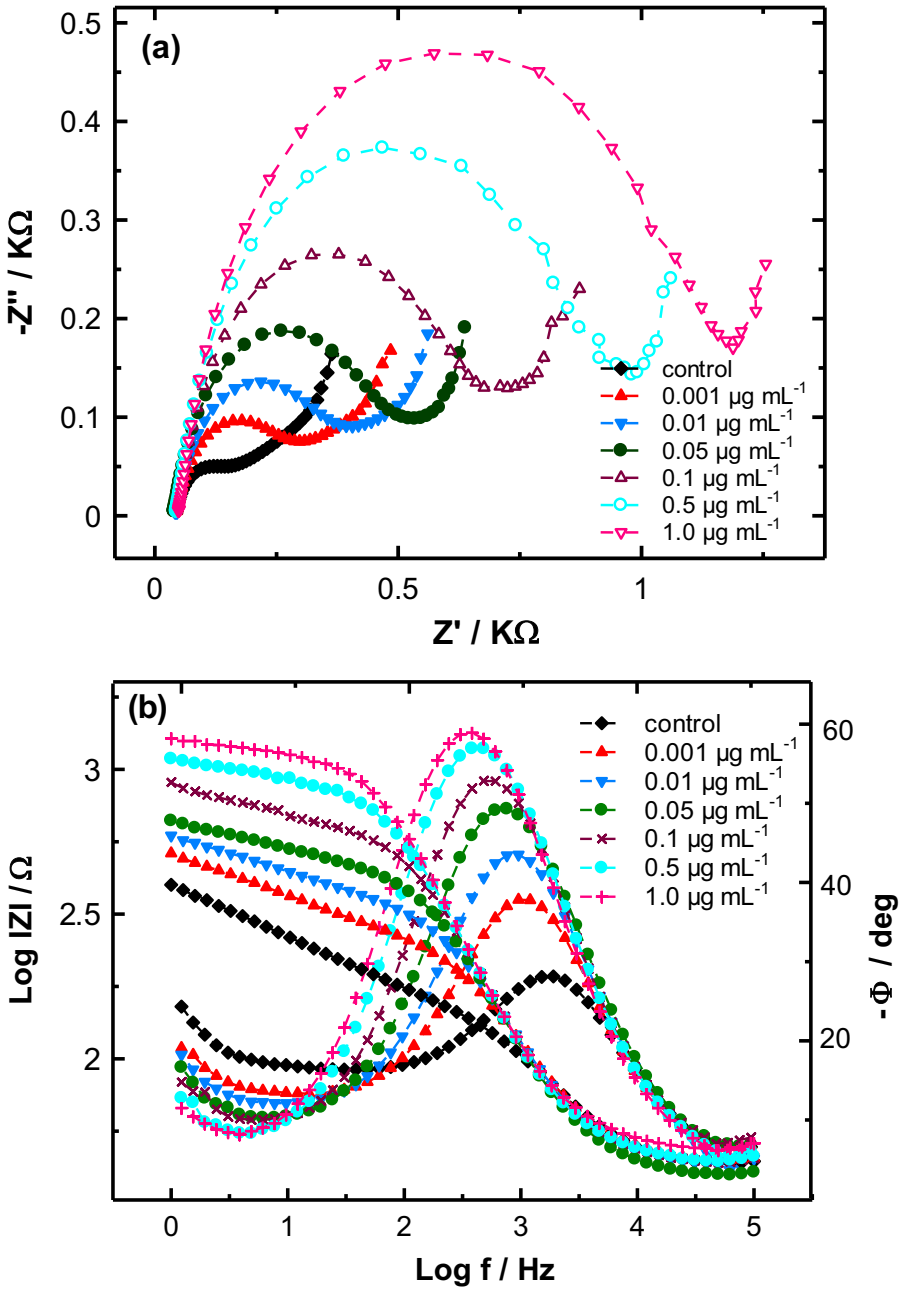

Fig. 7 **a** Faradaic impedance spectra of the bioelectrode in PBS (pH 7.4, 0.1 M KCl) solution containing 2 mM $[Fe(CN)_6]^{3-/4-}$ before and after incubation with different concentrations of Ag-cMb; **b** corresponding bode plot

impedance of the bioelectrode on immunoreaction were observed in the low frequency region <100 Hz where R_{et} is a dominant factor (Table 2), exhibiting good biocompatibility and sensitivity toward Ag-cMb.

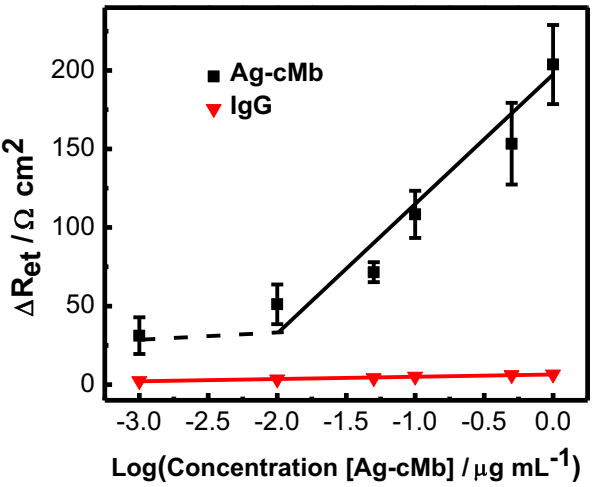

Fig. 8 Concentration-dependent calibration curve for bioelectrode; the *error bars* represent the standard deviation from three separate experiments

Figure 8 shows the linear calibration curve between change in the electron transfer resistance ($\Delta R_{et}=(R_{et})_{after\ immunoreactions}-(R_{et})_{control}$) and logarithmic value of Ag-cMb concentration in the range of 1.0 ng mL^{-1} to 1 μg mL^{-1}. Keeping in view the normal physiological range of Ag-cMb in human serum and the maximum cutoff level of myocardial infarction, EIS response of the bioelectrode was taken only up to 1 μg mL^{-1}. The linear R_{et} response of the bioelectrode can be represented by

$$\Delta R_{et}(\log[\text{Ag-cMb}]) = b\log[\text{Ag-cMb}] + 199.41 \quad (5)$$

The R_{et} sensitivity of the bioelectrode (i.e., slope of the calibration curve) was found to be 92.13 Ω cm^2 per decade of Ag-cMb with a correlation coefficient of 0.974 (n=5). Table 3 shows the comparative analytical performance of the bioelectrode with a few recently reported biosensors in literature for cMb detection. It is clear that this sensitivity of the AuNP-PPy-PPa-based bioelectrode is superior to the recently reported native PPy-PPa-based bioelectrodes,

Table 3 Comparative analytical performance of bioelectrode with existing electrochemical systems for Mb detection

Sensing technique	Transducing matrix	Linear response range	Limit of detection (ng mL^{-1})	Reference
Impedimetric	SAM/Au electrode	10^{-12}–10^{-6} M	15	[38]
Potentiometric	SAM of alkanethiol/ Au-coated Si chip	–	1,000	[39]
Square wave voltammetry	SPE/MeNP-DDAB/ anti-cMb	10–400 ng mL^{-1}	5	[40]
Flow injection/amperometry	Mb-MWNTs/GCE	1.78–53.4 μg mL^{-1}	353.98	[41]
Impedimetric	PPy-PPa/ITO	10–1,000 ng mL^{-1}	2.85	[23]
Impedimetric	AuNP-PPy-PPa/RGO/ APTES/ITO	10–1,000 ng mL^{-1}	1.49	Present work

[23] signifying the importance of the high electron transfer conduction characteristics of AuNP in a synergistic combination with PPy-PPa over RGO matrix.

Since specificity of the bioelectrode is of great importance to clinical diagnosis, the EIS response was also monitored with a nonspecific protein antigen, mouse Ag-IgG, under identical experimental conditions as described for Ag-cMb. A minute change in R_{et} response to Ag-IgG was observed over a concentration range of 1.0 ng mL^{-1} to 1 μg mL^{-1}, as depicted in Fig. 7, indicating the high specificity of the bioelectrode to Ag-cMb. The high sensitivity and specificity of the bioelectrode shows that it may be useful in clinical diagnostics after suitable optimization with human blood serum.

Conclusions

In this paper, we report the electrochemical polymerization of AuNP-PPy-PPa polymer nanocomposite film over RGO-modified ITO glass plate, as a biosensing platform for the detection of human cardiac biomarker, Ag-cMb. The RGO support offered excellent stability to the AuNP-PPy-PPa copolymer film, wherein the AuNP facilitated enhanced ionic and electronic transport ability of the polymer film. The protein antibody, Ab-Mb, was covalently immobilized to pendant carboxyl groups of AuNP-PPy-PPa/RGO through carbodiimide linkage and was characterized by various spectroscopic techniques. The porous and inhomogeneous surface morphology of the polymer nanocomposite film provided a large accessible surface area for a better probe orientation. The bioelectrode exhibited a linear impedimetric response to Ag-cMb in the range of 10 ng mL^{-1} to 1 μg mL^{-1}, in PBS (pH 7.4) in a low frequency region <100 Hz with a R_{et} sensitivity of 92.13 Ω cm^2 per decade of Ag-cMb. This high sensitivity and specificity of the bioelectrode suggests that the AuNP-PPy-PPa/RGO polymer nanocomposite can be used as a suitable biocompatible platform in device fabrication for clinical applications.

Acknowledgments We are grateful to Prof. R.C. Budhani, Director, National Physical Laboratory, New Delhi, India, for providing research facilities. One of the authors, Nidhi Puri, is thankful to CSIR for providing Senior Research Fellowship.

References

1. Dios, A. S. D., & Diaz-Garcia, M. (2010). *Analytica Chimica Acta, 666*, 1–22.
2. Singh, R., Premkumar, T., Shin, J., & Geckeler, K. (2010). *Chemistry A European Journal, 16*, 1728–1743.
3. Dong, L., Gari, R. R. S., Li, Z., Craig, M. M., & Hou, S. (2010). *Carbon, 48*, 781–787.
4. Li, Y. J., Gao, W., Ci, L. J., Wang, C. M., & Ajayan, P. M. (2010). *Carbon, 48*, 1124–1130.
5. Shao, Y. Y., Wang, J., Wu, H., Liu, J., Aksay, I. A., & Lin, Y. H. (2010). *Electroanalysis, 22*, 1027–1036.
6. Gan, T., & Hu, S. S. (2011). *Microchimica Acta, 175*, 1–19.
7. Wang, Y., Li, Y. M., Tang, L. H., Lu, J., & Li, J. H. (2009). *Electrochemistry Communications, 11*, 889–892.
8. Wang, C., Zhang, L., Guo, Z. H., Xu, J. G., Wang, H. Y., Zhai, K. F., & Zhuo, X. (2010). *Microchimica Acta, 169*, 1–6.
9. Shan, C. S., Yang, H. F., Han, D. X., Zhang, Q. X., Ivaska, A., & Niu, L. (2009). *Langmuir, 25*, 12030–12033.
10. Stankovich, S., Dikin, D. A., Dommett, G. H. B., Kohlhaas, K. M., Zimney, E. J., Stach, E. A., Piner, R. D., Nguyen, S. T., & Ruoff, R. S. (2006). *Nature, 442*, 282–286.
11. Muszynski, R., Seger, B., & Kamat, P. V. (2008). *Journal of Physical Chemistry C, 112*, 5263–5266.
12. Xu, C., Wang, X., & Zhu, J. W. (2008). *Journal of Physical Chemistry C, 112*, 19841–19845.
13. Shan, C. S., Yang, H. F., Han, D. X., Zhang, Q. X., Ivaska, A., & Niu, L. (2010). *Biosensors and Bioelectronics, 25*, 1070–1074.

14. Baby, T. T., Aravind, S. S., Arockiadoss, T., Rakhi, R. B., & Ramaprabhu, S. (2010). *Sensors and Actuators B: Chemical, 145*, 71–77.
15. Geim, A. K., & Novoselov, K. S. (2007). *Nature Material, 6*, 183–191.
16. Jiang, F., Yao, Z., Yue, R., Du, Y., Xu, J., Yang, P., & Wang, C. (2012). *International Journal of Hydrogen Energy, 37*, 14085–14093.
17. Ahuja, T., Mir, I. A., Kumar, D., & Rajesh. (2007). *Biomaterials, 28*, 791–805.
18. Geetha, S., Roa, C. R. K., Vijayan, M., & Trivedi, D. C. (2006). *Analytica Chimica Acta, 568*, 119–125.
19. Ghanbari, K., Bathaie, S. Z., & Mousavi, M. F. (2008). *Biosensors and Bioelectronics, 23*, 1825–1831.
20. Mishra, S. K., Pasricha, R., Biradar, A. M., & Rajesh. (2012). *Applied Physics Letters, 100*, 053701–053704.
21. Ren, F., Zhou, W., Du, Y., Yang, P., Wang, C., & Xu, J. (2011). *International Journal of Hydrogen Energy, 36*, 6414–6421.
22. Habibi, B., & Pournaghi-Azar, M. H. (2010). *International Journal of Hydrogen Energy, 35*, 9318–9328.
23. Puri, N., Mishra, S. K., Niazi, A., Biradar, A. M., & Rajesh, E. (2013). *Synthetic Metals, 169*, 18–24.
24. Weber, M., Rau, M., Madlener, K., Elsaesser, A., Bankovic, D., Mitrovic, V., & Hamm, C. (2005). *Clinical Biochemistry, 38*, 1027–1030.
25. Jaffe, A. S., Babuin, L., & Apple, F. S. (2006). *Journal of American College of Cardiology, 48*, 1–11.
26. Ng, S. M., Krishnaswamy, P., Morissey, R., Clopton, P., Fitzgerald, R., & Maisel, A. S. (2001). *American Journal of Cardiology, 88*, 611–617.
27. Torabi, F., Far, H. R. M., Danielsson, B., & Khayyami, M. (2007). *Biosensors and Bioelectronics, 22*, 1218–1223.
28. Mayr, B. M., Kohlbacher, O., Reinert, K., Sturm, M., Gröpl, C., Lange, E., Klein, C., & Huber, C. G. J. (2006). *Proteome Research, 5*, 414–421.
29. Zheng, Q., Liu, Z., & Cai, R. (2005). *Spectrochimica Acta Part A: Molecular and Biomolecular Spectroscopy, 61*, 1035–1038.
30. Sun, W., Li, L., Lei, B., Li, T., Ju, X., Wang, X., Li, G., & Sun, Z. (2013). *Materials Science and Engineering C, 33*, 1907–1913.
31. Yu, S., Cao, X., & Yu, M. (2012). *Microchemical Journal, 103*, 125–130.
32. Chang, H. H., Chang, C. K., Tsai, Y. C., & Liao, C. S. (2012). *Carbon, 50*, 2331–2336.
33. Sen, T., & Patra, A. (2009). *Journal of Physical Chemistry C, 113*, 13125–13132.
34. Wang, X., Song, L., Yang, H., Xing, W., Kandola, B., & Hu, Y. (2012). *Journal of Material Chemistry, 22*, 22037–22043.
35. Hsu, F.-H., & Wu, T.-M. (2012). *Synthetic Metals, 162*, 682–687.
36. Kong, J., & Yu, S. (2007). *Acta Biochimica et Biophysica Sinica, 39*, 549–559.
37. Klink, M. J., Iwuoha, E. I., & Ebenso, E. E. (2011). *International Journal of Electrochemical Science, 6*, 2429–2442.
38. Billah, M., Hays, H. C. W., & Millner, P. A. (2008). *Microchimica Acta, 160*, 447–454.
39. Wang, Y., Zhou, Y., Sokolov, J., Rigas, B., Levon, K., & Rafailovich, M. (2008). *Biosensors and Bioelectronics, 24*, 162–166.
40. Suprun, E. V., Shilovskaya, A. L., Lisitsa, A. V., Bulko, T. V., Shumyantseva, V. V., & Archakov, A. I. (2011). *Electroanalysis, 23*, 1051–1057.
41. Pakapongpan, S., Palangsuntikul, R., & Surareungchai, W. (2011). *Electrochimica Acta, 56*, 6831–6836.